Holistic characterization of an under-expanded high-enthalpy jet under uncertainty

Michele Capriati, Alessandro Turchi, Pietro Marco Congedo, Thierry E. Magin

Holistic characterization of an under-expanded high-enthalpy jet under uncertainty

M. Capriati,[1,2] A. Turchi,[1,3] P. M. Congedo,[2] and T. E. Magin[1,4]

[1)]*von Karman Institute for Fluid Dynamics, Waterloosesteenweg 72, 1640 Sint-Genesius-Rode, BE.*

[2)]*Inria, Centre de Mathématiques Appliquées, École Polytechnique, IPP, Route de Saclay, 91120 Palaiseau, FR.*

[3)]*Italian Space Agency, Science and Research Directorate, Via del Politecnico, 00133, Rome. Italy.*

[4)]*Aero-Thermo-Mechanics Laboratory, École Polytechnique de Bruxelles, Université Libre de Bruxelles, 1050 Brussels, Belgium.*

(*Electronic mail: michele.capriati@vki.ac.be)

(Dated: 17 May 2024)

Holistic characterization of an under-expanded high-enthalpy jet under uncertainty

Elaborate methodologies have been developed to study the thermo-chemical response of materials in high-enthalpy flows. To reach the high magnitudes of heat flux encountered in some hypersonic applications, one can resort to supersonic jets. They involve several physical effects, such as detached shocks ahead of probes. Because of these features, characterizing supersonic flows is a challenging task, especially when one accounts for experimental and modeling uncertainties. Building on the development of stochastic approaches, we propose a holistic methodology to determine the quantities of interest in an optimal fashion for an under-expanded high-enthalpy jet, using both experimental measurements and high-fidelity flow simulations. Given the high computational cost of the high-fidelity simulations needed to describe the flow, we built an adaptive/multi-fidelity surrogate model to replace the estimation of the costly computer solver. A Bayesian inference method then allowed for characterizing an experiment carried out in the von Karman Institute's Plasmatron facility, for which no robust methodology currently exists. We show that the reservoir pressure and temperature, and the nitrogen catalytic recombination coefficient of the copper probes can be accurately determined from the available measurements. Contrarily, the test conditions do not allow us to estimate the oxygen catalytic recombination coefficient. Finally, the characterized uncertainties are propagated through the numerical solver yielding an uncertainty-based high-fidelity representation of the hypersonic flow's structure variability.

I. INTRODUCTION

The determination of quantities of interest relevant to hypersonic applications, such as the flow free stream conditions or Thermal Protection Material (TPM) thermo-chemical properties, require accurate experimental measurements and high-fidelity flow simulations.

Supersonic high-enthalpy flows can be employed to characterize the response of TPMs under atmospheric entry conditions as they allow for obtaining high magnitudes of heat flux over TPM samples. Such flows can be produced both in Inductively Coupled Plasma (ICP)[1–3] and arc jet[4–6] facilities. For instance, an under-expanded plasma jet was employed by Sakharov[1] and Gordeev et al.[2] in the VGU-4 plasmatron to evaluate the heat flux and pressure evolution along the jet center line. Supersonic flows involve many physical effects[7,8], including complex shock structures and strong thermo-chemical non-equilibrium, and CFD tools become essential to describe the flow accurately. Because of these features, characterizing the testing environment is a challenging task, especially for what concerns the flow free stream enthalpy, as it is not directly accessible with the experimental set-up. Several procedures have been proposed for its characterization, including sonic throat or heat flux correlations[9–13], spectrometric measurements[9,14,15], and CFD simulations[9,16–18]. The last approach requires iterating the numerical enthalpy until the experimental heat flux is obtained. A fundamental assumption behind the methods relying on heat flux measurements concerns the catalytic coefficient used to model the surface of the calorimeter. Indeed, the heat flux is strongly dependent on the atomic recombination at its surface, which can be described using the catalytic efficiency of the material. Copper calorimeters are generally employed and assumed to be fully catalytic (efficiency greater than 0.1). However, large discrepancies about its value can be found in the literature. For example, Nawaz et al.[19] showed that the formation of an oxide layer lowered the catalytic efficiency to values as low as 0.01-0.03, and Viladegut and Chazot [20] reported a pressure-dependent efficiency, which turned out to be lower than 0.01 for gas pressure greater than 100 mbar. Since the catalytic efficiency of the calorimeters is not well-known, and its value directly affects the enthalpy characterization, its uncertainty should be adequately accounted for during the inference process.

The characterization of supersonic high-enthalpy flows requires a general and robust methodology that merges accurate measurements and multi-physics simulations while accounting for several sources of uncertainty. Uncertainty Quantification (UQ) techniques aim at characterizing

and potentially reducing such uncertainties. In uncertainty propagation studies, both modeling and experimental uncertainties are propagated through the solver to assess the uncertainty on the quantities of interest. Contrarily, in stochastic inverse problems, the uncertainty is propagated backward and the experimental data are exploited to characterize/reduce the uncertainty on selected model inputs. Bayesian analysis pertains to this class of problems. For example, state-of-the-art UQ methodologies were developed and applied for the material characterization in subsonic testing in the VKI Plasmatron[21–26]. In these studies, the subsonic nature of the flow allowed for reducing the dimension, and the cost, of the problem. The CFD solved the flow only along the stagnation line, making the UQ study very efficient. Contrarily, high-fidelity computations are needed to simulate supersonic jets. Diaz et al.[27] used high-fidelity computations to build a polynomial regression to characterize the arc jet nozzle inflow conditions as a function of the experimental heat flux and pressure. Brune et al.[28] also built a surrogate model on high-fidelity computations to perform a sensitivity study on the impact of uncertainty parameters on heat flux and pressure prediction on a probe in an arc jet.

UQ studies, either related to uncertainty propagation or inverse problems, are generally efficiently performed through surrogate models. These are trained on CFD computations and they mimic the response in terms of input-output relationship for a negligible computational cost. Polynomial chaos[29] or Kriging surrogate models[30] are widely used for this purpose. For example, in the work of Brune et al.[28] a polynomial chaos representation of the sample heat flux/pressure response was built considering 47 sources of uncertainty and 1500 high-fidelity CFD simulations were run to train and verify the surrogate model.

Even if associated only with the surrogate model training, the computational cost can be high. Multi-fidelity models[31–33] allow for lowering the computational effort by leveraging cheaper lower fidelity representations. The same can be achieved by using differently refined meshes in a multi-level formulation[32]. Multi-fidelity methods are recently gaining increasing and rapid attention over a wide range of fields[34–37], including aerospace applications[38–40]. Kriging methods are very suitable to be applied in a multi-fidelity framework: Co-Kriging[41,42] and Hierarchical Kriging[43] aims at combining different fidelity information to produce an accurate, but efficient, regression. Efficiency can be also increased by reducing to the minimum the number of training points, and successively enlarging the set by means of adaptive strategies[31,44].

In this work, we first present a supersonic experimental campaign recently conducted in the

VKI Plasmatron facility and provide a detailed flow analysis based on the high-fidelity solution obtained under nominal conditions. For the flow characterization, we propose a multi-fidelity-based Bayesian methodology. It aims at characterizing/reducing the uncertainties on the testing reservoir conditions and the catalytic efficiencies of the copper calorimeter used to measure the heat flux by exploiting the available experimental measurements. To the best of the authors' knowledge, it is the first time that a Bayesian technique that merges accurate measurements and high-fidelity simulations is applied to the characterization of a supersonic plasma flow. Given the costly nature of the high-fidelity simulations needed to describe the flow accurately, attention is focused on optimizing the methodology. A surrogate model is built by means of an adaptive/multi-fidelity strategy to improve efficiency while preserving accuracy. The third relevant result concerns the assessment of the variability of the flow structure, obtained by propagating the reservoir uncertainties through the numerical solver. Specifically, we are interested in assessing I) if the methodology allows for obtaining a robust characterization of the flow structure, and II) which flow feature, if any, is most sensitive to the reservoir conditions and their associated uncertainties. This might be useful in future experiments to determine whether performing additional measurements could result in an improved characterization. For example, if a specific flow structure is very sensitive to reservoir conditions, observing it might lead to a more robust flow characterization.

The article is structured as follows. In Section II the experimental campaign is presented as well as the methodology for its characterization. Section III illustrates the uncertainty quantification methodology followed in this paper. In Section IV, we describe the governing equations and the CFD solvers. Then, we illustrate the results of the high and low-fidelity solvers in the nominal conditions. Section V is then devoted to presenting the uncertainty-based results, on the characterization procedure and the high-fidelity estimation of the flow's structure variability. Finally, in Section VI the conclusion are drawn.

II. UNDER-EXPANDED HIGH-ENTHALPY JET: EXPERIMENT AND CHARACTERIZATION PROCEDURE

In this section, we first describe the experimental facility and the testing campaign. Secondly, we present the methodology employed for the flow characterization.

A. Plasmatron facility and experimental campaign

The VKI Plasmatron facility, sketched in Fig. 1, generates high-purity/high-enthalpy flows by means of a 160 mm diameter inductively coupled plasma torch powered by a high-frequency, high-power, high-voltage (400 kHz, 1.2MW, 2 kV) generator[45]. The facility is started with a gas of Argon, as it is easy to ionize. Once the plasma is stabilized, the gas is switched to the operating one (air, N_2 or CO_2). The gas exits in the test chamber, where vacuum pumps maintain the pressure to the operating value. A holder injects the test sample into the centreline of the plasma jet.

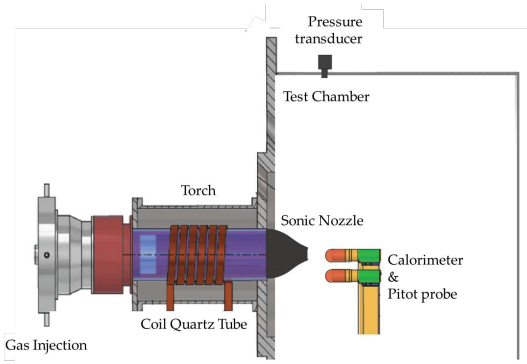

FIG. 1: Sketch of the Plasmatron facility, adapted from Fagnani et al.[46,a]

For flow characterization, a copper calorimeter can be inserted in the plasma jet to measure the cold wall heat flux at the stagnation point. It can be swapped with a Pitot probe, which allows for determining the stagnation pressure. Both probes are water-cooled: the temperature is kept around 350 K. The heat flux is retrieved by using the known water mass flow along with the measured temperature difference in the water at the inlet and the outlet of the calorimeter, which is measured by two type-E thermocouples. The chain leads to an uncertainty of 10% of the measurement[47,48]. The pressure is measured by a Validyne variable reluctance pressure transducer whose signal is amplified by a voltage demodulator. The uncertainty on the measurement is estimated to be 0.25% of the reading scale. The static pressure is assessed by means of an absolute pressure transducer, with uncertainty also of 0.25% of the reading scale. The mass flow rate is controlled by a rotame-

[a] Reprinted from *Measurement*, Vol. 227, A. Fagnani, B. Helber, A. Hubin, and O. Chazot, "Line-of-sight gas radiation effects on near-infrared two-color ratio pyrometry measurements during plasma wind tunnel experiments", p. 114175, Copyright (2024), with permission from Elsevier.

ter, with an accuracy of 5%.

The facility has been extensively used in subsonic regime for the characterization of catalytic and ablative materials[20,49–54]. Nevertheless, a convergent or a convergent/divergent nozzle can be attached at the torch exit to accelerate the flow to supersonic conditions[3,55,56]. This allows for maximizing the stagnation-point heat flux and the shape change of ablative samples.

In the studied configuration, the supersonic condition was achieved by accelerating the flow through a sonic nozzle, mounted at the exit of the plasma torch. The chamber pressure was lowered enough to generate a highly under-expanded jet. Specifically, the chamber pressure was set to 5.5 hPa, against a reservoir pressure of 165 hPa, resulting in a total pressure ratio of $\beta_0 = p_0/p_c = 30$. The sonic nozzle has an exit diameter of 35 mm and both probes were injected at a distance of 75 mm from the exit of the nozzle, before the occurrence of the Mach disk, after which the flow would become subsonic. The mass flow entering the plasma torch, measured through a rotameter, was 6 g/s, and the Plasmatron was supplied with an electrical power of 600 kW. These conditions allowed for reaching a target heat flux of 4.5 MW/m^2. Experimental means (μ) and uncertainties (2σ) are given in Table I.

TABLE I: Experimental uncertainty on the stagnation-point pressure and heat flux, p and q, mass flow rate, m, and total pressure at the entrance of the nozzle.

Quantity	μ	2σ
p, Pa	2500.0	50.0
q, MW/m^2	4.48	0.448
m, kg/s	6.0E-3	3E-4
p_0, Pa	16500.0	500.0

The supersonic jet is shown in Fig. 2. After the nozzle exit, the flow expands and accelerates to supersonic speed in the chamber, given its low pressure. A detached shock develops in front of the probe and interacts with a less visible barrel shock. The resulting transmitted shock is then reflected on the jet boundary. The flow structure will be discussed more in detail in Section IV A 3.

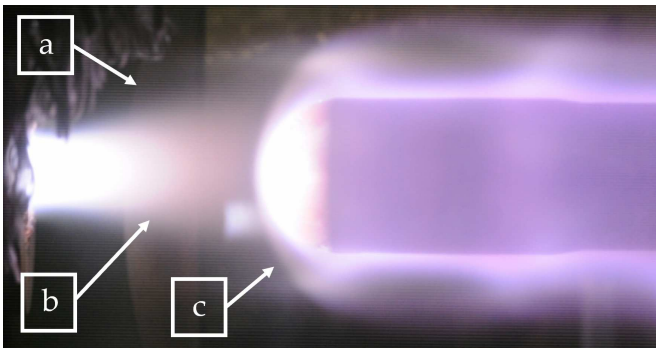

FIG. 2: Under-expanded air jet over a probe. (a) Jet boundary, (b) barrel shock, and (c) detached shock.

B. Formulation of the problem

The general objective of our work is the definition of an efficient and robust methodology to characterize the above-mentioned experimental campaign. Generally speaking, the flow at the exit of a sonic nozzle can be well characterized by the knowledge of the nozzle geometry, the gas total pressure (p_0) and temperature (T_0), and the chemical composition at the inlet of the nozzle. The total pressure, and the related experimental uncertainty, can be easily measured at the wall upstream of the nozzle, while the chemical composition, given the relatively high pressure and small velocity characterizing the inlet, can be safely computed at the equilibrium condition. On the other hand, the total temperature is not directly accessible and has to be characterized by means of auxiliary measurements. For example, downstream of the nozzle, typical experimental setups allow for measuring the stagnation point heat flux (q) and pressure (p). The mass flow rate in the nozzle (m), being controlled by a rotameter, is also known.

Based on the above description, we are interested in characterizing:

$$\boldsymbol{x} = [p_0, T_0, \gamma_{\mathrm{N}}, \gamma_{\mathrm{O}}], \tag{1}$$

given the experimental uncertainties on:

$$\boldsymbol{y} = [q^{\mathrm{exp}}, p^{\mathrm{exp}}, m^{\mathrm{exp}}]. \tag{2}$$

Note that, although the total pressure is experimentally measured, we imposed it as input to the inverse problem. This can potentially allow for reducing its associated uncertainty by exploiting

related measurements (e.g. stagnation-point pressure) and lead to a more robust characterization of the flow. Furthermore, besides the total quantities (p_0 and T_0), we are interested also in characterizing the catalytic efficiencies of the copper probe for nitrogen (γ_N) and oxygen (γ_O) recombination.

Bayesian inversion is a robust framework to characterize the quantities $\boldsymbol{x}$, given the uncertainty on the auxiliary quantities $\boldsymbol{y}$. Such a framework will be presented in Section III A. The analysis requires a mathematical model $\mathscr{M}(\boldsymbol{x})$, predicting the response $\boldsymbol{y}$ as a function of the quantities $\boldsymbol{x}$. Such a model is approximated by a surrogate model, described in Section III B 1, trained on high-fidelity simulations, presented in Section IV A 2. As we will see in the next section, the Bayesian analysis further requires the definition of prior distributions on the quantities to characterize. For these quantities that are not experimentally accessible, we prescribed non-informative uniform distributions, reported in Table II.

TABLE II: Non-informative uniform uncertainty for the total temperature at the entrance of the nozzle, T_0, and catalytic probabilities of the nitrogen and oxygen recombination, γ_N and γ_O.

Quantity	min	max
T_0, K	5600.0	8400.0
$\log_{10}\gamma_N$	-4	0.0
$\log_{10}\gamma_O$	-4	0.0

Note that we prescribed log-uniform distributions to the recombination efficiencies as their priors span several orders of magnitude.

III. UNCERTAINTY QUANTIFICATION METHODOLOGY

In this section, we first introduce the Bayesian inverse problem, and then we describe the construction of the surrogate model used to accelerate the computation of the likelihood.

A. Bayesian inverse problem

A Bayesian framework, sketched in Fig. 3, allows for characterizing the uncertainty on some quantities $\boldsymbol{x}$, for which we do not have experimental access, by means of complementary experimental observations $\boldsymbol{y}$.

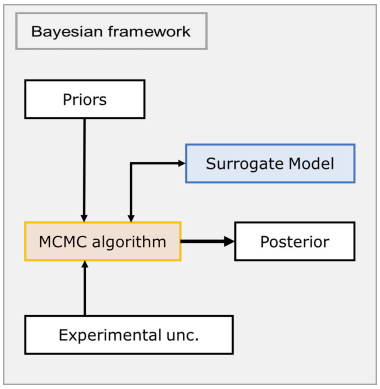

FIG. 3: Sketch of the Bayesian framework.

According to Bayes' theorem, the posterior distribution of $\boldsymbol{x}$ is:

$$\pi(\boldsymbol{x}|\boldsymbol{y}) = \frac{\pi(\boldsymbol{x})\pi(\boldsymbol{y}|\boldsymbol{x})}{\int \pi(\boldsymbol{x})\pi(\boldsymbol{y}|\boldsymbol{x})d\boldsymbol{x}}, \tag{3}$$

where $\pi(\boldsymbol{x})$ is the prior distribution of $\boldsymbol{x}$, $\pi(\boldsymbol{y}|\boldsymbol{x})$ is the likelihood of an observable quantity $\boldsymbol{y}$ given $\boldsymbol{x}$, and the integral at the denominator is the marginal likelihood or evidence, which ensures the distribution to integrate to 1. The first term represents what we know about $\boldsymbol{x}$ prior to performing the inversion, it can come from previous studies or expert judgment. The second term expresses how likely the realization $\boldsymbol{y}$ can be obtained by the input $\boldsymbol{x}$ through a numerical model $\boldsymbol{y} = \mathscr{M}(\boldsymbol{x})$, which expresses the experimental observations as a function of the quantities of interest that we intend to characterize.

In our study, we assume independence between the N_{obs} different experimental observations, and that the model error is negligible with respect to the experimental uncertainty, σ_i, on the measurement y_i. We further assume that the latter is normally distributed around the mean ($\mathscr{N}(0,\sigma_i^2)$). In this case, the likelihood reads:

$$\pi(\boldsymbol{y}|\boldsymbol{x}) = \prod_{i=1}^{N_{\text{obs}}} \mathscr{N}(y_i|\mathscr{M}_i(\boldsymbol{x}),\sigma_i^2). \tag{4}$$

Combining Eq. 3 and 4, it follows that the higher the experimental uncertainty on a given measurement is, the higher the posterior uncertainty on a calibrated parameter is expected to be.

It is generally difficult to compute analytically the evidence of Eq. (3). Hence, the posterior distribution is obtained by employing sampling methods such as the Markov Chain Monte Carlo (MCMC). Among others, the Metropolis-Hastings algorithm[57,58] allows for sampling from the posterior distribution without the need to compute the marginal likelihood.

The algorithm requires millions of calls to the forward model. Directly using high-fidelity simulations to this end is not efficient and one generally resorts to surrogate models. In fact, they are cheap mathematical approximations of the high-fidelity solver. Among those, Kriging models are widely used. Their construction will be described in Section III B 1. Nevertheless, there might be situations in which having enough high-fidelity solutions to build the surrogate model accurately can still be of prohibitive cost. Efficiency can be restored by employing multi-fidelity representations of the problem, adaptive sampling strategies, or a combination of the two. Although other multi-fidelity approaches can be used, including Polynomial chaos expansion[59–61] and Co-Kriging[41,42], we decided to employ the hierarchical Kriging formulation proposed by Han and Görtz[43]. It is described in Section III B 2, while, in Section III B 3, the adaptive sampling strategy adopted in this work is presented.

B. Surrogate model

1. Kriging

A surrogate model can be built for each observation y_i to speed up the MCMC algorithm. Let us assume we have a model $\mathscr{M}_i(\boldsymbol{x})$ providing the response y_i as a function of some input quantity $\boldsymbol{x}$. Let also assume we have n_s sampled points ($\mathscr{X} = \{\boldsymbol{x}^{(1)}, ..., \boldsymbol{x}^{(n_s)}\}$), and the corresponding model realizations ($\mathscr{Y}_i = \{y_i^{(1)}, ..., y_i^{(n_s)}\}$). A surrogate model can be trained on these pairs to provide the response at an untrained $\boldsymbol{x}$ point for a cheaper price. Kriging assumes $\mathscr{M}_i$ to be the realization of a Gaussian process:

$$\mathscr{M}_i(\boldsymbol{x}) \approx \mathscr{M}_i^K(\boldsymbol{x}) = \boldsymbol{\beta}_i^T \mathbf{f}_i(\mathbf{x}) + Z_i(\mathbf{x}). \tag{5}$$

The first term of the RHS is the process's mean, also called trend, whose unknown β_i parameters need to be determined. The second term Z_i is a stationary Gaussian process characterized by a variance σ_i^2. The stationary Gaussian process is defined by means of a correlation function ($R(x,x';\theta_i)$) between the points x and x'. Parameters σ_i^2 and θ_i also need to be determined. Once conditioning the process to the training points, one can compute the mean of the process, $\hat{\mathscr{M}}_i^K(\boldsymbol{x})$, at any untrained point, with confidence given by the process' standard deviation, $\hat{\sigma}_i(\boldsymbol{x})$.
Regarding the trend function, one may model it as a known regression function (simple Kriging), as an unknown regression constant (ordinary Kriging), or as a regression polynomial function (universal Kriging). In most cases, an *a priori* estimation of the trend function or its form is rather complex, and one generally opts for ordinary Kriging, relying on the stationary process to capture the model behavior. Nevertheless, when a model hierarchy can be defined, an estimation of the trend function can be obtained through a lower fidelity representation, as in the hierarchical Kriging formulation.

2. Hierarchical Kriging

Let us assume to have N_l different fidelity solvers, ranked from the lowest to the highest fidelity. In such a scenario, the Kriging surrogate model can be built in a hierarchical way, to reduce to the minimum the numerical effort of sampling solutions from the highest fidelity model.
The hierarchical Kriging, mathematically formulated by Han and Görtz[43], proposes to exploit the $l-1$ fidelity prediction ($\hat{\mathscr{M}}_i^{K,l-1}(\mathbf{x})$), scaled by a parameter β_i^l, as trend function for the l fidelity Kriging:

$$\mathscr{M}_i^{K,l}(\mathbf{x}) = \beta_i^l \hat{\mathscr{M}}_i^{K,l-1}(\mathbf{x}) + Z_i^l(\mathbf{x}) \tag{6}$$

After conditioning the Gaussian process on n_l training points, the l fidelity predictor, $\hat{\mathscr{M}}_i^{K,l}(\mathbf{x})$, is obtained. An exhaustive description of the formulation can be found in the work of Han and Görtz[43]. Its main advantages[35,43] are i) its efficiency and implementation ease: it does not require a cross-correlation function to be built, as for co-Kriging modeling; being one Kriging evaluated per fidelity it demands the inversion of N_l correlation matrices of size $n_l \times n_l$ in spite of a $n_s \times n_s$ matrix, which is advantageous for computer performing; ii) training points independence, i.e., the set of lower fidelity training points does not require the inclusion of the high-fidelity ones; and iii) ease of application of infill techniques, i.e., its Gaussian variance is well suited for adaptive sampling.

3. Adaptive sampling

Efficiency can be further enhanced by reducing to the minimum the number of training points, and successively enlarging the set, only where necessary, by means of adaptive sampling strategies. When working in a multi-fidelity framework, one is not only interested in sampling in the stochastic space but also in having a criterion to establish which fidelity level to refine. For this reason, we slightly modified the strategy proposed by Zhang et al.[62]. Since the low-fidelity prediction is scaled by a β factor, the low-fidelity uncertainty should be scaled by the same factor, such that:

$$\hat{\sigma}_i^2(\boldsymbol{x},l) = \begin{cases} (\beta_i^{hf}\hat{\sigma}_i^{lf}(\boldsymbol{x}))^2 & \text{if l = low-fidelity} \\ (\hat{\sigma}_i^{hf}(\boldsymbol{x}))^2 & \text{if l = high-fidelity} \end{cases}. \tag{7}$$

Zhang's work concerns an optimization problem, thus, the Expected Improvement (EI) was maximized:

$$(\boldsymbol{x},l) = \text{argmax } EI_{vf}(\boldsymbol{x},l). \tag{8}$$

Contrary, in the present work, we want to rely on more than 2 fidelity models, and adaptively explore the high-fidelity one. Following Zhang's work, it makes sense to scale the l fidelity variance, by the products of the l scaling factors that separate it from the high-fidelity one:

$$\hat{\sigma}_i^2(\boldsymbol{x},l) = \begin{cases} (\prod_{j=l+1}^{N_l}(\beta_i^j)^2)(\hat{\sigma}_i^l(\boldsymbol{x}))^2 & \text{if l} \neq \text{high-fidelity} \\ (\hat{\sigma}_i^{hf}(\boldsymbol{x}))^2 & \text{if l = high-fidelity} \end{cases} \tag{9}$$

Furthermore, for exploring purposes, we want to train where the standard deviation is maximum:

$$(\boldsymbol{x},l) = \text{argmax } \hat{\sigma}_i(\boldsymbol{x},l) \tag{10}$$

In Appendix A, we propose two algebraic examples to verify the efficiency of the method.

C. Strategy implementation

The surrogate model was built in a multi-fidelity/adaptive way. The whole procedure is simplified in the scheme on the right side of Fig. 4: I) the lowest fidelity (δ) is computed according to a cheap representation of a problem, described in Section IV C. The other three fidelity, γ, θ, and α, rely on the high-fidelity computational model, presented in Section IV A, but made use of 3 differently refined grids, characterized by a different numerical uncertainty, see Section IV B.

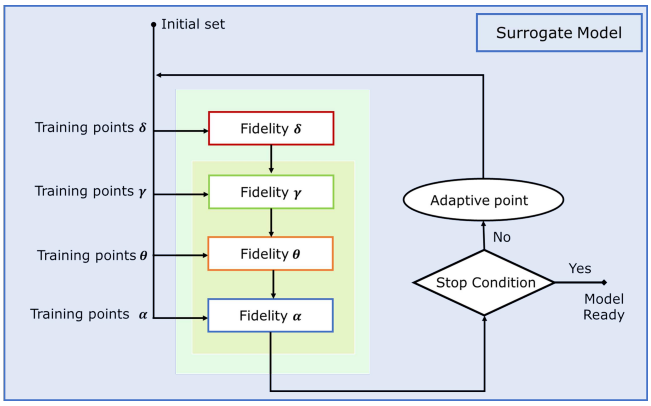

FIG. 4: Sketch of the multi-fidelity adaptive surrogate model construction.

First, an ordinary Kriging was built by means of the δ low-fidelity training points. Following, a hierarchical Kriging was progressively trained for fidelity γ, θ, and α using the corresponding l-fidelity CFD points and the $l-1$-fidelity surrogate representation. An initial coarse training point data set was chosen and enriched, where necessary, by means of an adaptive strategy, detailed in Section III B 3, to assess statistical convergence. Both the inverse problem and the surrogate model construction are performed by means of the software UQLAB[63], where the hierarchical Kriging implementation is very straightforward[35,64].

IV. GOVERNING EQUATIONS, SIMULATIONS WITH HIGH-FIDELITY/LOW-FIDELITY MODELS

We simulated the flow from the exit of the plasma torch to the probe location. Preliminary simulations indicate the flow to be out of thermal equilibrium after the sonic nozzle. However, such simulations also show that in the studied conditions thermal non-equilibrium and turbulence effects have minimal influence on the quantities of interest (namely ~1.5% on the stagnation-point heat flux and ~2.5% on the stagnation-point pressure). Thus, the flow was assumed to be steady, laminar, and in thermal equilibrium. We also assumed the surface of the probes to be partially catalytic.

We solved chemical reacting Navier-Stokes equations of an air mixture of five species, S=[N_2,

O_2, NO, N, O], in thermal equilibrium:

$$\frac{\partial \rho_i}{\partial t} + \nabla \cdot (\rho_i \boldsymbol{u} + \boldsymbol{j}_i) = \dot{\omega}_i, \quad \forall i \in [1, ..., n_s], \tag{11}$$

$$\frac{\partial \rho \boldsymbol{u}}{\partial t} + \nabla \cdot (\rho \boldsymbol{u} \otimes \boldsymbol{u} + p\bar{\bar{I}} + \bar{\bar{\tau}}) = \boldsymbol{0}, \tag{12}$$

$$\frac{\partial \rho E}{\partial t} + \nabla \cdot (\rho \boldsymbol{u} H + \bar{\bar{\tau}} \cdot \boldsymbol{u} + \boldsymbol{q}) = 0. \tag{13}$$

Symbol ρ_i is the partial density of species i, $\boldsymbol{j}_i$ its diffusion mass flux, $\dot{\omega}_\mathrm{i}$ its chemical production/destruction rate, $\boldsymbol{u}$ is the mass-averaged mixture velocity, n_s the number of species, p the thermodynamic pressure of the mixture, $\bar{\bar{\tau}}$ the viscous stress tensor, E the total energy, $H = E + p/\rho$ the total enthalpy, and $\boldsymbol{q}$ the total heat flux. Thermodynamics properties were obtained using the NASA polynomials[65]. Diffusion mass fluxes were computed using the self-consistent effective binary diffusion models[66], while viscosity and thermal conductivity according to the Gupta-Yos mixture rule[67]. The chemical production rates, $\dot{\omega}_i$, were obtained imposing the rate coefficients from Park et al.[68].

The probe acts as a catalyst for the recombination of atomic nitrogen and oxygen impinging on its surface. The recombination reaction is exothermic and its contribution to the total heat flux must be taken into account. The set of surface reactions and heat exchange can be numerically expressed as a Boundary Condition (BC). In this study, such a BC was provided through MUTATION^{++}[69,70]. When the surface temperature is known, an isothermal condition can be used and the wall composition is obtained by solving the surface mass balance for each species i, which for a catalytic material reads:

$$\dot{\omega}_i = \boldsymbol{j}_i \cdot \boldsymbol{n}, \quad \forall \mathrm{i} \in [1, n_s]. \tag{14}$$

Versor $\boldsymbol{n}$ is the normal to the surface. The system (14) is solved by means of a Newton method and the surface state is returned to the CFD solver. In this work, we used a phenomenological approach to describe the chemical source term. This rather simple approach only requires the definition of the probability that a macroscopic reaction takes place:

$$\gamma_i = \frac{\mathscr{N}_i^{rea}}{\mathscr{N}_i}, \tag{15}$$

where $\mathscr{N}_i^{rea}$ is the number flux of species i subject to the reaction and $\mathscr{N}_i = n_i \sqrt{k_\mathrm{B} T_\mathrm{s} / (2\pi m_i)}$, the number flux of species i impinging the surface. The symbol k_B stands for Boltzmann's constant,

T_s the surface temperature, and m_i, the mass of species i. A fully catalytic behavior is obtained when the probability approaches unity; a non-catalytic behavior when it is equal to zero, partial catalysis lies between these two bounds. The chemical production rate reads:

$$\dot{\omega}_i = m_i \gamma_i^r \mathcal{N}_i. \tag{16}$$

Two different codes were used to simulate the flow: a high-fidelity one, described in Section IV A, and a low-fidelity one, presented in Section IV C.

A. High-fidelity simulations

In this section, after presenting the high-fidelity CFD solver and the BC imposed for the simulations, we analyze the numerical flow structure and the grid convergence of the quantities of interest.

1. US3D solver

US3D is a three-dimensional finite-volume high-fidelity flow solver developed at the University of Minnesota for aerodynamic/hypersonic applications[71]. The solver is highly scalable and efficient, making it possible to solve very large problems on parallel computers in a cost-effective manner. In this work, we computed the numerical fluxes according to the modified Steger-Warming scheme[72] with a MUSCL approach to obtain second-order accuracy. The full matrix point relaxation[73] was used for the time integration. The catalytic BC condition was provided through MUTATION^{++}, previously coupled to US3D[74,75].

2. High-fidelity numerical domain and boundary conditions

The physical domain was discretized as shown in Fig. 5a; from the left, in a clockwise direction, we can see the I) exit of plasma torch/nozzle inlet, II) sonic nozzle surface, III) expansion chamber, and IV) probe. Particular attention was posed to well capture the shock to have reliable results on the probe surface, as shown in Fig. 5b. Particularly, we cut the left domain of the chamber using a quarter of circumference to improve the alignment of the mesh to the shock. We remark that such a cut is not expected to affect the solution, as this area is not characterized by gradients of the flow quantities. Four grids, listed in Table III, are obtained by systematically doubling the number of

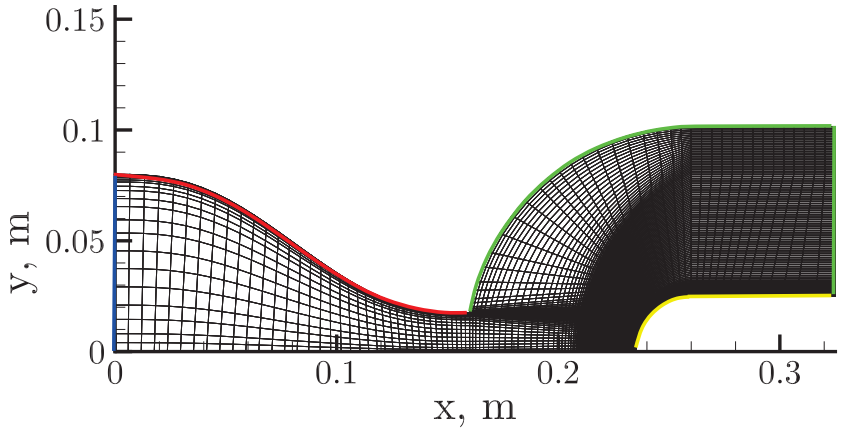

(a)

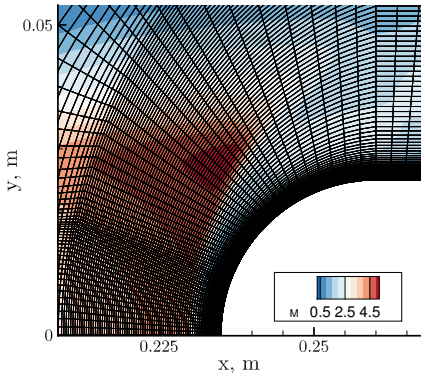

(b)

FIG. 5: Details of mesh III of Table III: (a) numerical domain, from the left, in the clockwise direction: I) exit of plasma torch/nozzle inlet (in blue), II) sonic nozzle surface (in red), III) expansion chamber (in green), and IV) probe (in yellow); (b) zoom of the numerical domain in the shock region, the grid is aligned to the shock.

the nodes in both the x and y directions to assess the grid convergence.

Regarding the simulation BCs, the total temperature and pressure were imposed at the nozzle inlet. Here, the chemical composition was assumed to be at equilibrium. The nozzle surface

TABLE III: Details of the meshes used: index, number of cells, length of the first cell at the stagnation point (Δn), normalized characteristic mesh (h_i), and time to converge (t_CPU).

Index	Cells	Δn, m	h_i	t_CPU, min
I	172224	5E-7	1	≈ 1600
II	43056	1E-6	2	≈ 200
III	10764	2E-6	4	≈ 30
IV	2691	4E-6	8	≈ 4

was characterized by a non-reacting isothermal condition (whose temperature was kept constant at 1500 K for all the simulations). The chamber surface was characterized by an inlet condition for numerical stability imposing a small horizontal velocity (1 m/s), room temperature, and a chamber pressure of 5.5 hPa (also these conditions were kept constant for all the simulations). The probe was modeled as an isothermal/catalytic surface, solving a surface mass balance through MUTATION^{++}. A temperature of 350 K was imposed. Finally, a supersonic outlet condition was prescribed on the exit section; all the other surfaces were characterized by a symmetry BC.

The values of the total temperature and pressure at the nozzle entrance, and of the recombination probabilities on the catalytic probe were set according to the training points, as will be discussed in Section V. In the following, we will describe the results obtained under nominal conditions ($T_0 = 7500$ K, $p_0 = 16500$ Pa, $\gamma_\mathrm{N} = 0.0736$, and $\gamma_\mathrm{O} = 0.1170$). The nominal catalytic efficiencies were taken from Bellas[76].

3. Flow structure

Two high-fidelity numerical representations of the experiment, based on nominal conditions ($T_0 = 7500$ K, $p_0 = 16500$ Pa, $\gamma_\mathrm{N} = 0.0736$, and $\gamma_\mathrm{O} = 0.1170$), are given in Fig. 6 to illustrate the flow features: the undisturbed flow on the top, and the probe-disturbed one at the bottom. The flow structure is rather complex, particularly:

(a) a Prandtl-Meyer expansion fan develops at the exit of the nozzle to expand the flow to the chamber pressure;

(b) a jet boundary separates the jet from the quiescent chamber gas;

(c) a barrel shock deviates the streamlines to align them to the jet boundary;

(d) a Mach disk, characteristic of highly under-expanded jet, is generated because of the oblique shock irregular reflection;

(e) a reflected shock develops at the triple point (red circle) where the barrel shock intersects the Mach disk.

(f) a detached shock appears before the Mach disk because of the inference of the intrusive probe. Behind it, the flow expands because of the body's curvature. The detached shock interacts with the barrel one. The transmitted detached shock is then reflected on the jet boundary, deviating it.

The temperature profile along the stagnation line was extracted from the two simulations; it is shown in Fig. 7. As one can see in Fig. 6 and 7, being the flow supersonic, the disturbance does not travel upstream and the structure of the flow in the undisturbed and disturbed case is nearly identical up to the edge of shock. Thus, we can safely characterize the nozzle inlet conditions by intrusively probing the flow.

The temperature and Mach contours are respectively shown at the top and the bottom of Fig. 8. The flow first accelerates in the nozzle to the sonic condition, and then it continues the expansion in the chamber, reaching a peak Mach number of around 4.5, just before the detached shock. It re-accelerates behind it. Contrarily, the temperature drops during the expansion and sharply increases in the shock layer. Both the boundary layer developing along the nozzle wall and the jet boundary are characterized by an extended temperature gradient, which explains the thick density gradient in these regions observed in Fig. 6.

It is also worth analyzing the chemistry of the flow. Despite the temperature drop, the flow appears to be chemically frozen through the whole expansion, as shown in Fig. 9, due to the pronounced velocity gradients. Strong diffusion is visible across the jet boundary, where the dissociated gas meets the quiescent one, mostly characterized by molecules at room temperature. The atomic nitrogen and oxygen mass fractions profiles, as well as the temperature one, were extracted along the central line and shown in Fig. 10. As one can see, the atoms recombine in the boundary layer developing in front of the probe, mostly driven by surface catalysis. The atomic

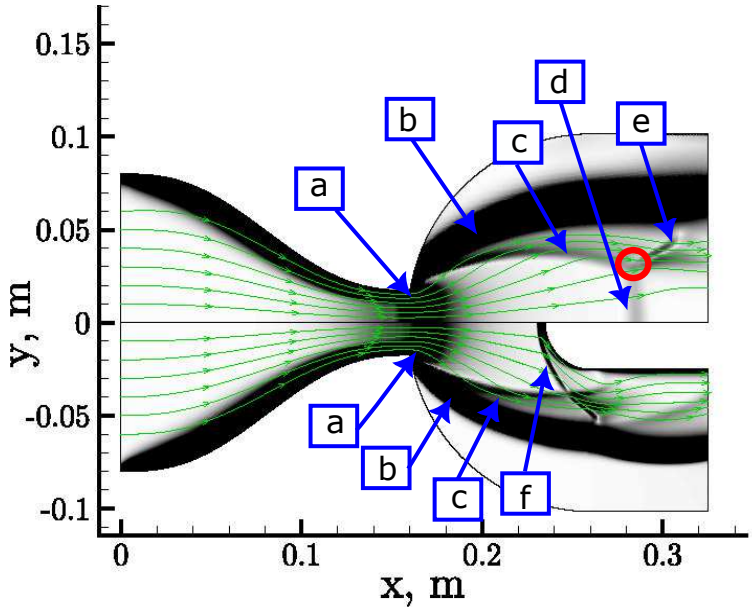

FIG. 6: Numerical flow structure obtained with a total temperature of 7500 K and a total pressure of 16500 Pa imposed at the entrance of the sonic nozzle. Density gradient contours. (a) Prandtl-Mayer expansion fan, (b) Jet boundary, (c) Barrel shock, (d) Mach disk, (e) Reflected shock, and (f) Detached shock. The triple point with a red circle.

nitrogen also partially recombines along the nozzle wall boundary layer because of homogeneous chemistry driven by the decrease in the temperature.

B. Numerical uncertainty

All the numerical simulations were performed on a numerical grid and they are thus affected by a numerical error, which was characterized following the procedure proposed by Eça and Hoekstra[77]. The numerical error reads:

$$\varepsilon_\phi \approx \delta_{\mathrm{RE}} = \phi_i - \phi_0 = \alpha h_i^p. \tag{17}$$

The quantity ϕ_i is a flow quantity of interest at the grid refinement i, ϕ_0, the estimate of the exact solution, α, a constant to be determined, h_i, the typical cell size and p is the observed order of

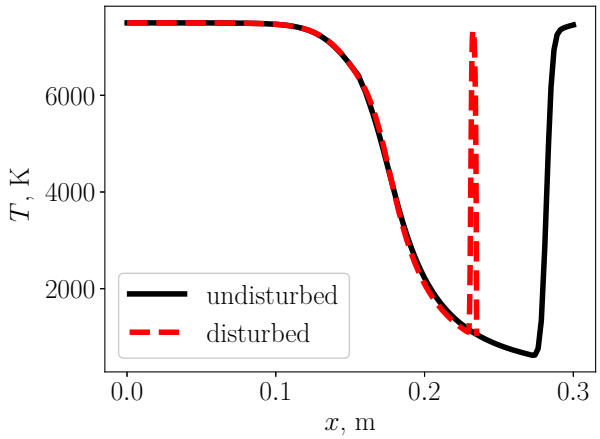

FIG. 7: Distribution of temperature along the jet central line: profile of the undisturbed flow in solid black line, probe-disturbed one in dashed red lines. The flow is nearly identical up to the edge of the shock.

grid convergence. In most applications, the exact solution of the quantity of interest cannot be analytically computed; in these cases, it can be estimated as the asymptotic limit for the element size approaching the infinitesimal value. Hence, the quantity of interest at the refinement i can be approximated as:

$$\phi_i = \phi_0 + \alpha h_i^p. \tag{18}$$

By using a minimum of four nested meshes, the values α, p, and ϕ_0 can be estimated by minimizing the standard deviation, σ, between the numerical solutions and the fit law in Eq. (18). A positive value of the order of convergence (p) implies a monotonic convergence, in contrast, a negative value a monotonic divergence.

Still according to the work[77], the uncertainty on the prediction associated with the mesh at the refinement i reads:

$$U_\phi(\phi_i) = \begin{cases} F_s \varepsilon_\phi(\phi_i) + \sigma + |\phi_i - \phi_{\text{fit}}|, & \text{if } \sigma < \Delta_\phi \\ 3\frac{\sigma}{\Delta_\phi}(\varepsilon_\phi(\phi_i) + \sigma + |\phi_i - \phi_{\text{fit}}|), & \text{otherwise} \end{cases} \tag{19}$$

where $\Delta\phi = (\phi_i^{\max} - \phi_i^{\min})/(n_g - 1)$ is a data range parameter and F_s is a safety factor equal to 1.25 if $0.5 < p < 2.1$ and $\sigma < \Delta\phi$, and to 3 otherwise.

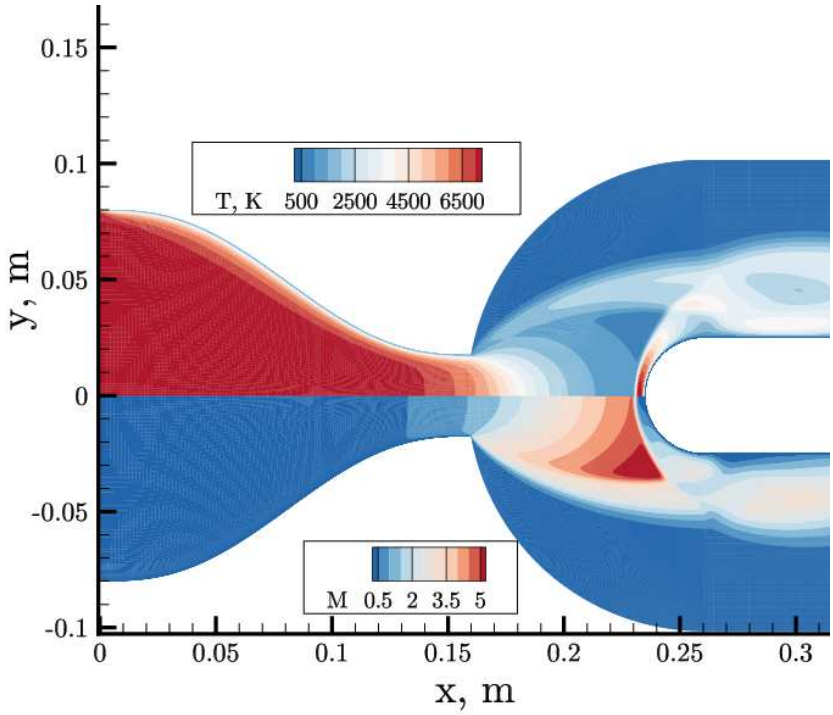

FIG. 8: Temperature (top) and Mach (bottom) contours. The flow expands reaching a Mach number of around 4.5 before the shock. The temperature drops during the expansion and increases at the shock layer.

The nominal conditions were also imposed to characterize the numerical uncertainty associated with each of the four meshes reported in Table III. The obtained order of convergence, asymptotic value, and numerical uncertainty of Mesh I are reported in Table IV for the stagnation-point pressure and heat flux, as well as for the nozzle mass flow rate. The experimental uncertainty on these observables is also given in the same table.

The dependency of the results versus the grid refinement for the three observables is shown in Fig. 11. The coarse solutions are characterized by high numerical uncertainty, which reduces refining the grid. Specifically, as one can see in Table IV, the Mesh I has a numerical uncertainty that is lower than the experimental one for all the observables, making it a very accurate representation of the problem. As we will discuss in the next section, one may use many simulations on

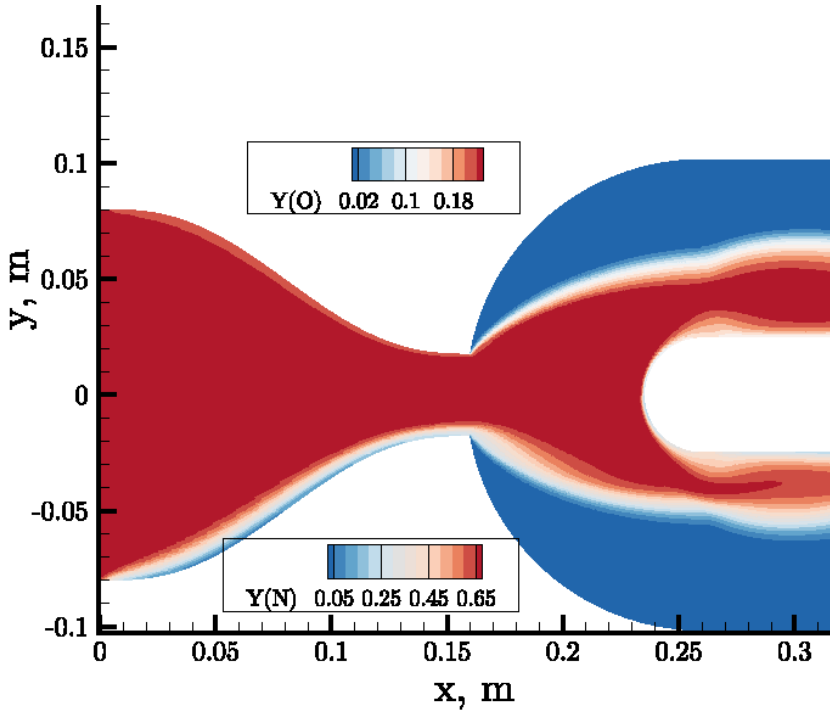

FIG. 9: Mass fractions contours: atomic oxygen (top) and atomic nitrogen (bottom). The flow is chemically frozen through the whole expansion.

TABLE IV: Results of the grid convergence study performed on the meshes in Table III for the stagnation-point pressure and heat flux, p and q, and the mass flow rate, m. For each observable: order of convergence, p, asymptotic value, ϕ_0, numerical uncertainty of Mesh I, U_1, and experimental uncertainty, $2\sigma_{exp}$.

Observable	p	ϕ_0	U_1	$2\sigma_{exp}$
p, Pa	1.57	2436.90	38.57	50
q, W/m^2	1.57	4.48E6	7.5E4	4.48E5
m, kg/s	0.55	5.8E-3	1.1E-4	3E-4

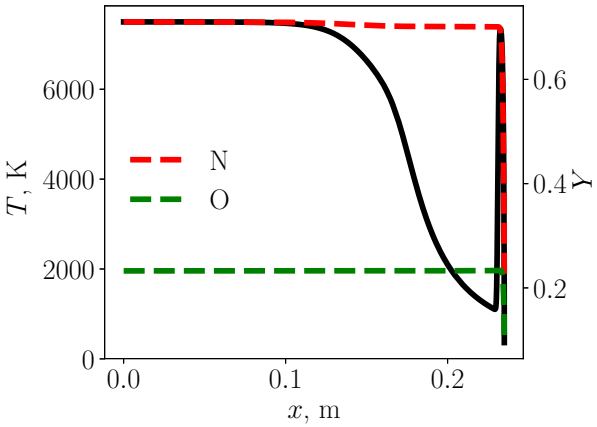

FIG. 10: Temperature (left) and mass fractions (right) distribution along the jet center line, from the nozzle inlet to the probe stagnation point. The flow partially recombines in the boundary layer, mostly driven by the catalysis of the probe surface.

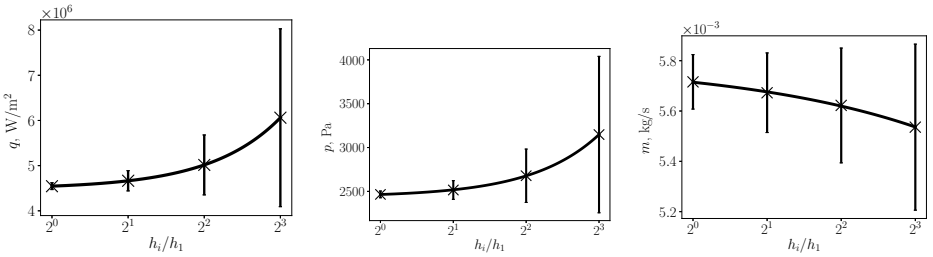

(a) (b) (c)

FIG. 11: Grid convergence study for the (a) stagnation-point heat flux, (b) stagnation-point pressure, and (c) nozzle mass flow rate. Cross: CFD value; solid line: fit law according to Eq. (18); bars: numerical uncertainty according to Eq. (19).

the efficient, but less accurate, Mesh IV to train a surrogate model, retaining fewer simulations on Mesh I for accuracy purposes.

We also remark that all the simulations were run until the steady-state solution was achieved. The convergence was assessed by monitoring the root mean square density residual, which decreased by at least five orders of magnitude in each simulation, resulting in a negligible iterative

Holistic characterization of an under-expanded high-enthalpy jet under uncertainty

error.

C. Low-fidelity simulations

A low-fidelity solver was built to compute the field along the stagnation line and the pressure and heat flux at the stagnation point of the probe. First, we compute the state of the gas just before the detached shock in front of the probe, as sketched in Fig. 12. The geometrical throat area,

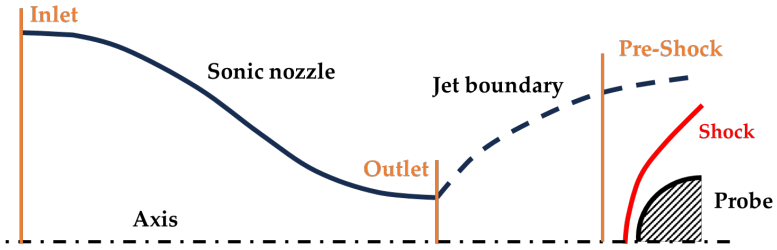

FIG. 12: Sketch of an under-expanded jet over a probe.

together with the sonic condition at the exit of the nozzle, the conservation of total enthalpy and pressure, and frozen chemistry are imposed to compute the nozzle's choked mass flow and the gas state at the outlet, for a given reservoir condition. After that, the state of the gas before the shock is computed imposing the previously computed mass flow and the total enthalpy and pressure conservation. The jet diameter before the detached shock, needed to compute the gas state, was computed as a function of the reservoir pressure, whose law was calibrated based on three US3D simulations performed on a relatively coarse mesh.

Once the pre-shock state is known, one can compute the post-shock flow properties employing the jump relations, and the stagnation-point pressure and heat flux through correlations[12,78–80]. However, such correlations assume the chemistry of the flow to be either frozen or in equilibrium and the probe surface either fully- or non-catalytic. To relax these assumptions, we preferred to simulate the flow from the pre-shock point to the stagnation point with an in-house CFD code[81] equipped with specific catalytic BCs. It solves dimensionally reduced Navier-Stokes equations along the stagnation line. Input of the simulation are the flow free-stream velocity, temperature, and partial densities, which are obtained with the above-mentioned procedure. The code also requires the definition of the free-stream velocity gradient ($\beta = \partial v/\partial y$) as input. It was also

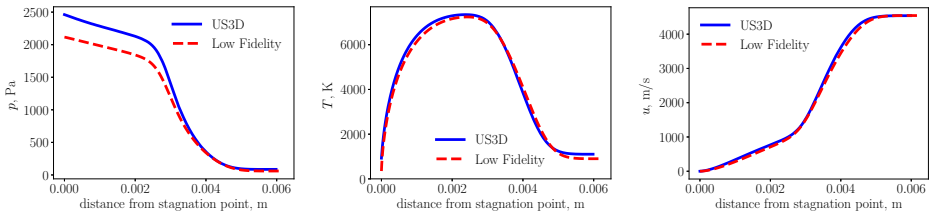

FIG. 13: Comparison between the high-fidelity solution extracted along the stagnation line (US3D), and the low-fidelity one: (a) pressure, (b) temperature, and (c) normal velocity.

computed as a function of the reservoir pressure, whose law was calibrated based on the three US3D simulations used for calibrating the jet diameter. On the surface, the code solves the same surface-mass balance used for the high-fidelity simulations through MUTATION^{++}. Output of the code are the stagnation-point pressure and heat flux.

The method was verified by comparing the US3D solution extracted along the stagnation line and the low-fidelity one, obtained with the above-mentioned procedure. The two different solutions are plotted in Fig. 13. As one can see, the solution is well approximated. Nevertheless, the value of the stagnation pressure, and of the stagnation-point heat flux, turned out to be lower than the high-fidelity ones, probably due to some two-dimensional effects (e.g. the flow under-expansion and the jet structure) that were not accounted for. However, we remind that we make use of this procedure to compute a good approximation of the quantities of interest, being the accuracy guaranteed by the high-fidelity simulations. We finally remark that the whole procedure takes around one minute to converge (one-quarter of the time required by a US3D simulation on the coarsest mesh), allowing us to cost-efficiently capture the input-output dependency.

V. UNCERTAINTY-BASED RESULTS

In this section, we first introduce the construction of the surrogate model, which was trained on the deterministic simulations performed by means of both the low- and high-fidelity solvers presented in the previous section, then, we present the results of the flow characterization. Finally, we assess the variability of the flow structure by propagating both the prior and the posterior

distributions of the total pressure and temperature at the entrance of the nozzle.

A. Surrogate model construction

We first built a surrogate model, which expresses the observables $\boldsymbol{y} = [q^{\text{exp}}, p^{\text{exp}}, m^{\text{exp}}]$ as a function of $\boldsymbol{x} = [p_0, T_0, \gamma_{\text{N}}, \gamma_{\text{O}}]$, on the stochastic space reported in Table I and II. Such a step is essential to perform a Bayesian inversion, as the latter requires millions of calls to the forward model. The surrogate model, which approximates the CFD response for a much lower computational cost, allowed us to efficiently solve the inverse problem.

In previous works from del Val et al.[24,25] and Turchi et al.[21,22], a low-fidelity CFD solver was employed to simulate a subsonic flow obtained in the Plasmatron and efficiently train the surrogate model. However, the previously discussed compressible features of the supersonic case cannot be described using a low-fidelity solver and high-fidelity simulations must be employed. This gain in accuracy comes at the expense of efficiency, which is not ideal when working in a UQ framework. The method efficiency was restored by building the surrogate model in an adaptive/multi-fidelity fashion.

The surrogate model is constructed as sketched in Fig. 4. The lowest-fidelity model (δ) is the cheap representation of the problem described in Section IV C. The other three fidelity, γ, θ, and α, rely on US3D computations on three differently refined grids, namely Mesh IV, III, and I, characterized by a different numerical uncertainty, as discussed in Section IV B. First, an ordinary Kriging was built by means of the δ low-fidelity training points. Then, a hierarchical Kriging was progressively trained for fidelity γ, θ, and α using the corresponding l-fidelity CFD training points and the $l-1$-fidelity surrogate representations as trend.

The initial number of training points was chosen by balancing the computational cost of each model's fidelity and our computational resources. A large number of training points ($N_\delta = 160$) was set for the inexpensive δ fidelity, a moderate number ($N_\gamma = 20$ and $N_\theta = 20$) for the γ and θ fidelity, and only $N_\alpha = 5$ for the expensive α fidelity. Another $N_{\text{v}} = 5$ independent points on the α fidelity were computed for verification purposes.

The training set was then adaptively refined employing the Kriging standard deviation of the heat flux model, using the method outlined in Section III B 3. A normalized error was introduced as:

$$NRMSE = \sqrt{\frac{\sum_{i=0}^{N_{\text{v}}} (Y_{\text{v},i} - \hat{Y}_i)^2}{N_{\text{v}}}} \frac{100}{\max Y_{\text{v},i} - \min Y_{\text{v},i}}, \tag{20}$$

to evaluate the accuracy of the surrogate model ($Y_{v,i}$ indicates the CFD estimate, while $\hat{Y}_i$ the Kriging prediction). The *NRMSE* on the heat flux decreased from 1.874% to 0.4936% sampling a total of 82 δ, 26 γ, and 24 θ training points. This set of points was further enriched with 3 α points to get a *NRMSE* on the pressure and on the mass flow rate prediction respectively of the 0.43196% and of the 0.22846%. Since the *NRMSE* was below the 0.5% for all the surrogate models, they were considered accurate and their uncertainties (also on average below the 0.5%) were not accounted for during the inverse problem.

It is worth noting that most of these points were added on the border of the four-dimensional hypercube, as shown in Fig. 14. This is expected by exploring techniques. In fact, since the initial training points were mostly sampled in the interior of the input space and the model response is nearly linear, the borders of the hypercube are characterized by the highest uncertainty. Anyway, we remark that the majority of the added points were obtained employing the cheap δ model, with a relatively null impact on the overall computational cost.

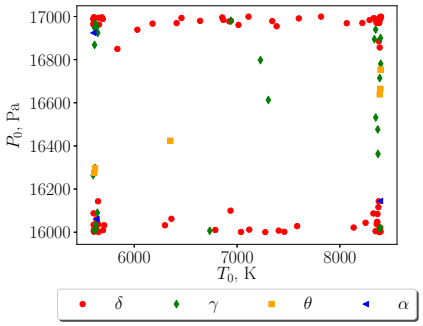

FIG. 14: Added points: the majority of the points were sampled on the border of the hypercube.

The gain in accuracy obtained by employing lower-fidelity simulations in a hierarchical fashion is highlighted in Fig. 15, where the model predictions on the heat flux are plotted against the CFD verification values.

The red crosses in the plot refer to the predictions of a surrogate model trained only on high-fidelity points. As one can see, the crosses depart by the 45-degree line, indicating that the surrogate model mispredicts the response. One way to improve the accuracy to satisfactory values would be by increasing the number of high-fidelity points. However, this would lead to a dramatic increase in the computational burden owing to the computational cost of each high-fidelity simulation.

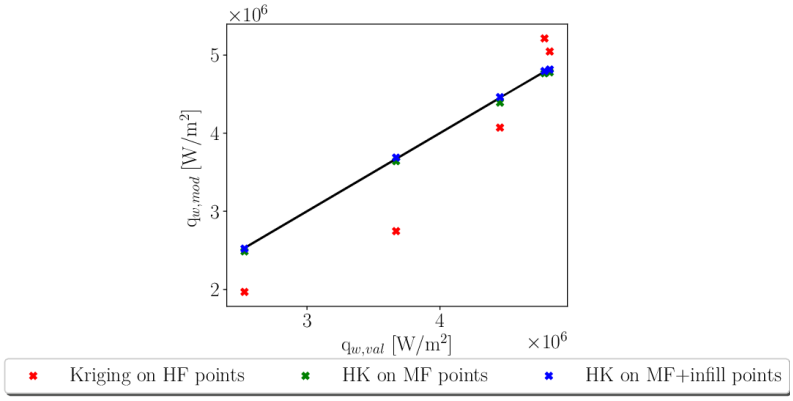

FIG. 15: QQplot: CFD response VS Surrogate model response. Points from the adaptive/multi-fidelity surrogate model on the 45-degree line.

On the other hand, the construction of the multi-fidelity surrogate model allowed us to obtain good accuracy and preserve efficiency. In fact, its predictions, shown with green crosses in the same figure, almost lie on the 45-degree line.
Further increase in accuracy was achieved by employing the adaptive sampling strategy. It is evident on the same plot: these predictions, plotted with blue crosses, perfectly lay on the 45-degree line.

B. Flow characterization

The verified surrogate model was then employed to perform the Bayesian inversion. A total of 10 MCMC chains characterized by 10^5 iterations were generated. The first 20% of the points of each chain was neglected as Burn-In. The multivariate potential scale reduction factor, computed with Gelmen-Rubin diagnostic[82,83], is $R = 1.0035$, ensuring that the chain is well converged.

The posterior marginals relative to the four quantities of interest are plotted in Fig. 16. Specifically, the reservoir's total temperature probabilistic density presents a well-defined peak at 7000 K, with a standard deviation of around 300 K, leading to a coefficient of variation ($CV = \sigma/|\mu| \cdot 100$) of the 4.28%. The reservoir's total pressure probability density is Gaussian-shaped, with a mean of around 16730 Pa, and a standard deviation of 140 Pa ($CV = 0.84\%$). Interestingly, we almost

halved the experimental uncertainty by using complementary measurements. The copper probe's nitrogen catalytic efficiency turned out to be also well-characterized, with a probability density peak value of around 0.15, and support ranging from 0.01 to 1. These values are in agreement with those found by del Val et al.[26] in a study performed on a subsonic test in the Plasmatron, where copper's γ_N and γ_O were inferred using the same variable. On the other hand, it was not possible to characterize the efficiency of the oxygen recombination. In fact, in the studied conditions, the atomic oxygen fraction is much lower than the atomic nitrogen one, see Fig. 10. Hence, also the associated fraction of heat released during the recombination process is lower compared to the fraction released by the nitrogen reaction, making it impossible to use the heat flux measurement for its estimation.

The actual value of the fraction of heat released during the recombination primarily depends on the thermo-chemical condition of the gas at the entrance of the nozzle and the catalytic coefficients of the surface. For example, under the nominal conditions introduced in Section IV, the diffusive heat flux due to nitrogen recombination is estimated to be 1.9 MW, more than three times higher than the one due to oxygen recombination, 0.54 MW. To better characterize the oxygen catalytic efficiency, one should perform an experiment at a lower inlet temperature, in a range where oxygen is dissociated, but nitrogen is mostly in molecular form.

The joint distribution of γ_N and γ_O is plotted in Fig. 17. As one can see, the two quantities of interest are correlated and a characterization of the oxygen recombination coefficient would improve also the characterization of the nitrogen one.

C. Flow structure variability

In this section, we investigate the variability of the flow structure. To this end, the prior and posterior distributions on the total pressure and temperature at the entrance of the nozzle (p_0, T_0) were propagated to investigate the variability of the flow structure. An algorithm was written to automatically detect the compressible features in each simulation. It follows a series of steps:

1. from the solution field, the stagnation line and 24 vertical lines are extracted in the range $x = [0.16 - 0.27]$ m.

2. The points belonging to the jet boundary, the barrel shock, and the detached shock are identified by detecting the relative maxima in the density gradient lines. The reconstructed

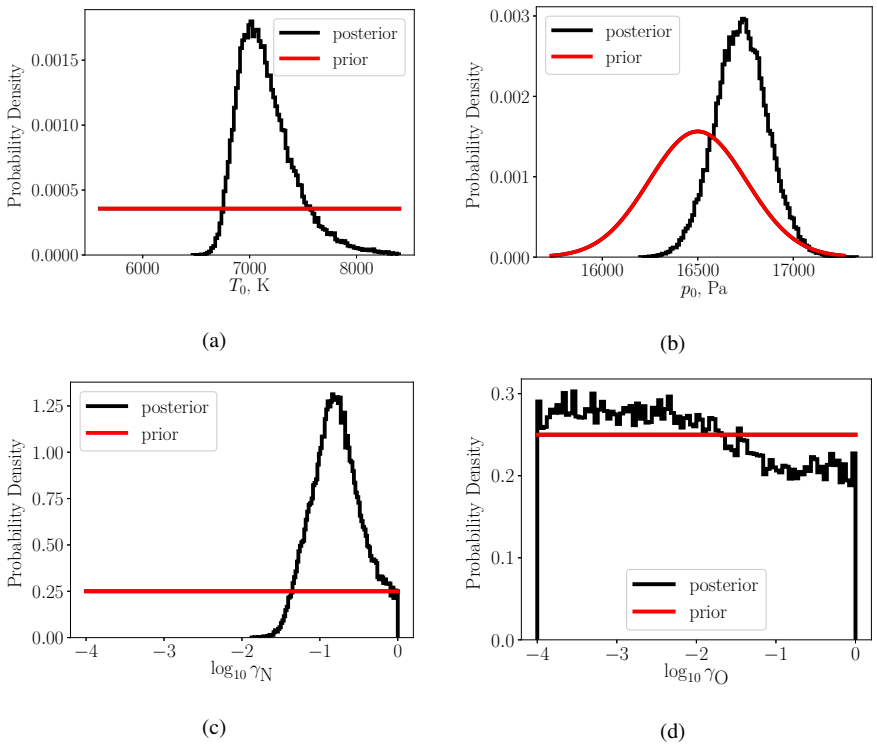

FIG. 16: Prior and posterior marginal distributions for (a) total temperature, (b) total pressure, (c) nitrogen recombination, and (d) oxygen recombination.

points are shown in Fig. 18.

3. The reconstructed points are then fitted for two reasons: I) to reduce the noise in the features, and II) to obtain the fit coefficients, which are more convenient to construct a surrogate model and to propagate the uncertainties. Two different fits are performed to reconstruct the detached shock: the first up to the point in which it intersects the barrel shock, and from here to $x = 0.27$ m, as its shape changes at the intersection point. The jet boundary, the barrel shock, and the second part of the detached shock were fitted with a third-order polynomial. The term $\sqrt{x - x_{\text{shock}}}$ was added to the polynomial used to fit the first part of the detached shock to enforce a vertical tangent at the shock location.

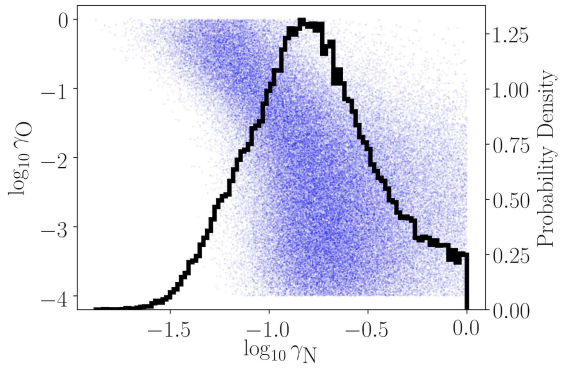

FIG. 17: Joint distribution of γ_O and γ_N.

4. The stand-off distance is computed as the difference between the x coordinate of the relative maximum of the density gradient along the stagnation line, before the increase in the boundary layer, and the coordinate of the stagnation point.

5. The coordinates of the point in which the detached shock intersects the barrel shock are computed as the point in which the fit of the detached shock intersects the one of the barrel shock.

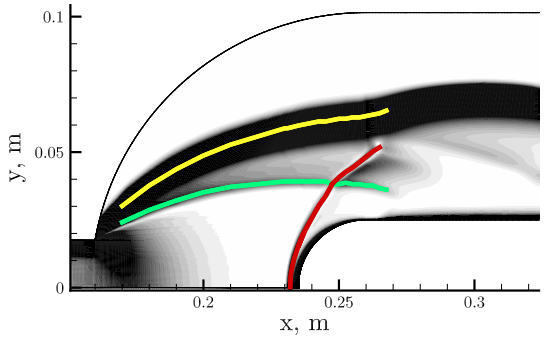

FIG. 18: Reconstructed points belonging to the jet boundary (plotted in yellow), the barrel shock (in green), and the detached shock (in red).

A surrogate model was built for the coefficients of the fits of each compressible feature, for the coordinates of the intersection point, and for the stand-off distance. We performed other 15 high-

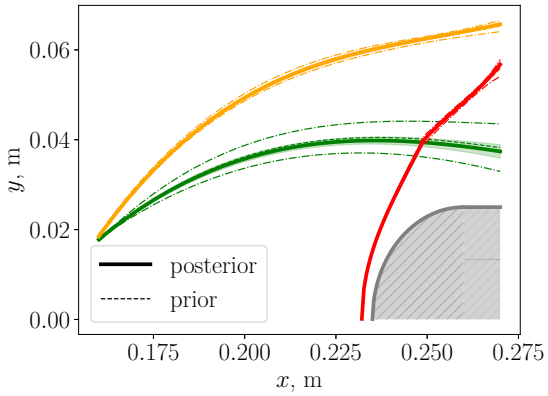

FIG. 19: Prior and posterior uncertainty on the flow structure: jet boundary (in orange), barrel shock (in green), and detached shock (in red). Prior: mean of the propagation plotted with dashed line, bounded by dash-dotted lines indicating the 95% interval of confidence. Posterior: the continuous line represents the mean, while the shadow areas represent the uncertainty within the 95% of confidence.

fidelity simulations to improve the quality of the surrogate model. The simulation inlet conditions were randomly sampled from the reduced posterior distribution.

Both the prior and the posterior distributions were then propagated through the surrogate models. The propagated uncertainties on the flow structure are shown in Fig. 19. As one can see, the barrel shock exhibits the largest variability with respect to the inlet conditions. This gets dramatically reduced when the total pressure and temperature are characterized. The same holds true also for the jet boundary and the detached shock, although the differences are much less pronounced. We can better appreciate the improvement in the predictions of these features by looking at Fig. 20a and Fig. 20b, where the shock stand-off distance and the intersection point variability are respectively shown. The most likely distance of the shock from the stagnation point increases from 2.90 mm to 2.95 mm when we characterize the inlet conditions, while the associated uncertainty decreases from $\sigma = 0.06$ mm ($CV = 2.08\%$) to $\sigma = 0.038$ mm ($CV = 1.29\%$). Likewise, the uncertainty in the intersection location is greatly reduced.

Overall, the characterization of the inlet conditions yields a much more robust prediction of the flow structure.

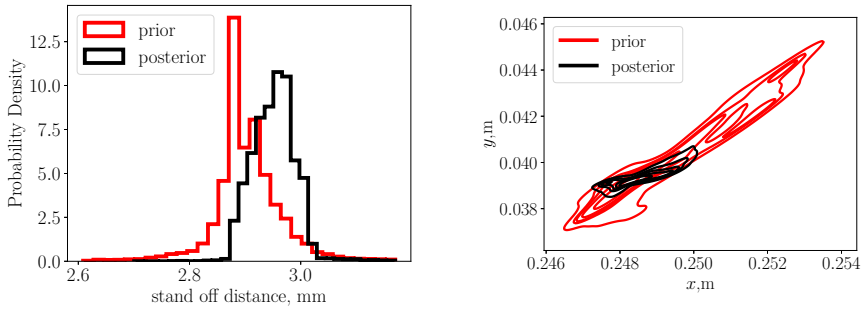

(a) (b)

FIG. 20: Prior (in red) and posterior (in black) uncertainties on the (a) stand-off distance, and (b) the intersection point.

VI. CONCLUSIONS

We presented a recent supersonic experimental campaign conducted in the VKI Plasmatron facility and provided a detailed description of the flow, based on CFD simulations. Then, we proposed a new methodology to characterize the testing conditions of supersonic high-enthalpy flows, for which a robust procedure did not exist. Specifically, we presented a multi-fidelity-based Bayesian framework that accounts for experimental and modeling uncertainties and relies on high-fidelity simulations to describe the flow accurately. We applied such a methodology to reduce the uncertainties on the testing free-stream conditions and the probe catalytic efficiencies exploiting complementary experimental observations. Considering the large number of calculations needed to perform the UQ study, and their associated computational cost, we built an adaptive/multi-fidelity surrogate model to mimic the high-fidelity CFD response. The initial set of training points was further enriched by an exploring infill strategy. Verification tests highlighted the gain in accuracy obtained by constructing the Kriging surrogate model leveraging lower-fidelity representations. Once verified, the surrogate model was employed to solve the stochastic inverse problem. As opposed to forward propagation studies, the Bayesian framework allows for exploiting experimental measurements to characterize the uncertainty on targeted quantities. In fact, the Bayesian analysis revealed pronounced peaks for the probability density of the total temperature and total pressure at the entrance of the sonic nozzle, yielding a robust characterization of the test conditions with a coefficient of variation below the 4.3%. Another important outcome of this study was

the determination of the nitridation catalytic efficiency of the copper calorimeter used to measure the heat flux. Nevertheless, given the relatively small amount of atomic oxygen versus atomic nitrogen present in the flow, it was not possible to estimate the oxygen recombination efficiency. The reservoir uncertainties were also propagated to assess the robustness of the prediction of the flow structure. The barrel shock exhibited the greatest variability with respect to the total pressure and temperature, suggesting that future experiments should address the measurement around this structure to characterize the reservoir conditions better. It was also observed that the uncertainty on the barrel shock gets largely reduced when the total pressure and temperature are characterized. The same holds for the shock stand-off distance and for the point at which the detached shock intersects the barrel one.

Finally, we remark that the proposed methodology is general and that including additional experimental measurements in the inference is relatively straightforward. Thus, we strongly believe that the proposed methodology should be systematically applied to characterize supersonic experimental campaigns.

ACKNOWLEDGMENTS

The authors acknowledge the Air Force Office of Scientific Research (AFOSR) for supporting the work under the grant FA9550-18-1-0209. The authors warmly thank Andrea Fagnani and Bernd Helber for their insights on the experimental campaign.

DATA AVAILABILITY STATEMENT

The data that support the findings of this study are available within the article.

Appendix A: Verification algebraic examples

Following, we propose two algebraic examples to verify the efficiency of the method.

a. 1D Algebraic Verification Test Case

The Forrester function[42] is employed to test the hierarchical Kriging with the proposed adapting sampling strategy. It consists of two fidelity, namely $\mathscr{M}^{\alpha}(x)$, and $\mathscr{M}^{\delta}(x)$. Two further fidelity were added, $\mathscr{M}^{\theta}(x)$, and $\mathscr{M}^{\gamma}(x)$, to mimic the four-fidelity form that we intend to use in our work. Furthermore, we assumed a fictitious computational cost, t^*_{CPU}, in line with the one observed for the corresponding CFD simulations. The four functions are:

$$\begin{cases} \mathscr{M}^{\alpha}(x) = (6x-2)^2 \sin(12x-4) & t^*_{\mathrm{CPU}} = 1600 \\ \mathscr{M}^{\theta}(x) = 1.9\mathscr{M}^{\alpha}(x) + 2.5 & t^*_{\mathrm{CPU}} = 30 \\ \mathscr{M}^{\gamma}(x) = 4.\mathscr{M}^{\alpha}(x) + 5.5 & t^*_{\mathrm{CPU}} = 4 \\ \mathscr{M}^{\delta}(x) = 0.5.\mathscr{M}^{\alpha}(x) + 10x - 10 & t^*_{\mathrm{CPU}} = 1 \end{cases} \tag{A1}$$

A normalized error between the high-fidelity prediction and the real function is computed as:

$$NRMSE = \sqrt{\frac{\sum_{i=0}^{N_{\mathrm{v}}} (\mathscr{M}^{\alpha}(x_i) - \hat{\mathscr{M}}^{\alpha}(x_i))^2}{N_{\mathrm{v}}}} \frac{100}{\max(\mathscr{M}^{\alpha}(x_i)) - \min(\mathscr{M}^{\alpha}(x_i))},$$

where N_{v} is the number of validation points, and $\hat{\mathscr{M}}^{\alpha}(x_i)$ is the multi-fidelity model prediction at the validation points. A total of 1000 equally-spaced points were used for validation. The initial surrogate model was built on 6 δ training points, and 3 training points for the remaining fidelity, sampled in the range [0,1] with an LHS technique; 15 more points were adaptively added. The whole experiment was run 200 times to avoid the verification being influenced by initial *lucky* or *unlucky* points. The results were averaged on the 200 repetitions.

The exercise showed that an average of 10.9 points were added in the efficient δ model, and 1.34 and 1.28 on the medium γ and θ fidelity. Only an average of 1.45 points were sampled from the α model. The statistical convergence history averaged on the 200 repetitions, is plotted in Fig. 21: the normalized error dropped from a value of 19.7% to 0.32%. The difference in performance is evident when we compare this result to the one we would get using the same equivalent computational cost only on high-fidelity LHS points: we could have afforded only an average of around 4.55 LHS training points, which would lead to an $NRMSE = 17.48\%$. To achieve a comparable error of 0.35% we would need 20 LHS high-fidelity training points, corresponding to a computational cost of more than four times higher.

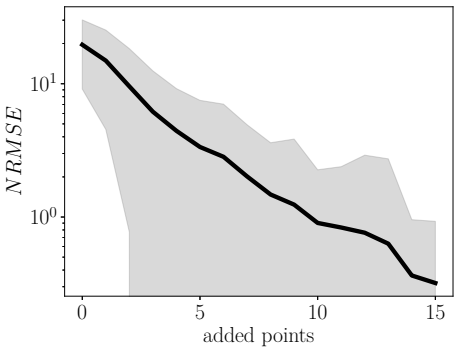

FIG. 21: Statistical convergence history for adaptive sampling: mean (solid line) plus and minus one standard deviation (shadow area).

b. 4D Algebraic Verification Test Case

A second test was performed using a four-dimensional input space and four models characterized by a different fidelity. The high-fidelity function was built to mimic the stagnation-point heat flux computation (as the sum of a conductive, dependent on the cube of the velocity and the square root of the density, and a diffusive part, dependent on the partial densities and the recombination efficiencies of oxygen and nitrogen) , while the lower fidelity to imitate the numerical error. Also in this case, we assumed a fictitious computational cost, equal to the one of the previous test. The four functions are:

$$\begin{cases} \mathscr{M}^{\alpha}(x,y,z,w) = x^3\sqrt{y} + y(0.2z + 0.8w) & t^*_{\text{CPU}} = 1600 \\ \mathscr{M}^{\theta}(x,y,z,w) = 1.9\mathscr{M}^{\alpha} + 2.5 & t^*_{\text{CPU}} = 30 \\ \mathscr{M}^{\gamma}(x,y,z,w) = 4.\mathscr{M}^{\alpha} + 5.5 & t^*_{\text{CPU}} = 4 \\ \mathscr{M}^{\delta}(x,y,z,w) = 0.5\mathscr{M}^{\alpha} - 10 + 10x^2\sqrt{y} + y(0.1z + 0.2w) & t^*_{\text{CPU}} = 1 \end{cases}$$

A total of 10^4 LHS points were used for validation. The initial surrogate model was built on 6 δ training points, and 3 training points for the remaining fidelity, sampled in the range [1,5] with an LHS technique; 50 more points were adaptively added. The whole experiment was run 200 times and the results averaged on the 200 repetitions.

The exercise showed that an average of 26.335 points were added in the efficient δ model, and 7.3 and 6.865 on the medium γ and θ fidelity. Only an average of 9.5 points are sampled from the

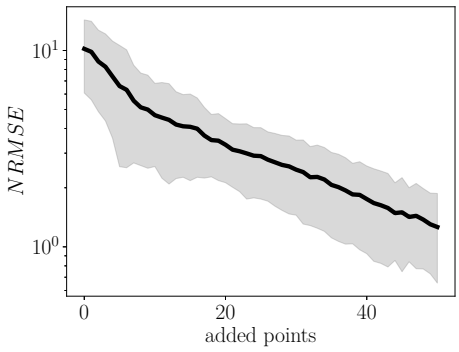

FIG. 22: Statistical convergence history for adaptive sampling: mean (solid line) plus and minus one standard deviation (shadow area).

high-fidelity model. The statistical convergence history averaged on the 200 repetitions, is plotted in Fig. 22: the normalized error dropped from a value of 10.19% to 1.26%. The difference in performance is evident when we compare this result to the one we would get using the same equivalent computational cost only on high-fidelity LHS points: we could have afforded only an average of around 12.73 LHS training points, which would lead to an $NRMSE = 3.31\%$. To achieve a comparable error of 1.27% we would need 28 LHS high-fidelity training points, corresponding to a computational cost of more than two times higher.

REFERENCES

[1]V. I. Sakharov, "Numerical simulation of thermally and chemically nonequilibrium flows and heat transfer in underexpanded induction plasmatron jets," Fluid Dynamics **42**, 157–168 (2007).

[2]A. Gordeev, A. Kolesnikov, and V. Sakharov, "Flow and heat transfer in underexpanded nonequilibrium jets of an induction plasmatron," Fluid Dynamics - FLUID DYN **46**, 623–633 (2011).

[3]D. Le Quang, Y. Babou, O. Chazot, and P. Andre, "Investigation of supersonic air plasma jet produced in the vki plasmatron facility," ESA Special Publication **714**, 31 (2012).

[4]C. Purpura, F. De Filippis, P. Barrera, and D. Mandanici, "Experimental characterisation of the cira plasma wind tunnel scirocco test section," Acta Astronautica **62**, 410–421 (2008).

[5]U. Duzel, O. Schroeder, H. Zhang, and A. Martin, "Numerical simulation of an arc jet test

section," Journal of Thermophysics and Heat Transfer **34**, 393–403 (2020).

[6]A. Balter-Peterson, F. Nichols, B. Mifsud, and W. Love, "Arc jet testing in NASA ames research center thermophysics facilities," in *AlAA 4th International Aerospace Planes Conference* (American Institute of Aeronautics and Astronautics, 1992).

[7]E. Franquet, V. Perrier, S. Gibout, and P. Bruel, "Free underexpanded jets in a quiescent medium: A review," Progress in Aerospace Sciences **77**, 25–53 (2015).

[8]R. Muraoka and T. Hiejima, "Onset conditions for Mach disk formation in underexpanded jet flows," Physics of Fluids **34**, 116125 (2022).

[9]C. Park, G. Raiche, D. Driver, J. Olejniczak, I. Terrazas-Salinas, T. Hightower, and T. Sakai, "Comparison of Enthalpy Determination Methods for an Arc-Jet Facility," Journal of Thermophysics and Heat Transfer **20**, 672–679 (2006).

[10]C. Shepard, F. Milos, and J. Taunk, "A sonic flow equation for electric arc jets," in *24th Plasma Dynamics, and Lasers Conference* (American Institute of Aeronautics and Astronautics, 1993).

[11]R. Pope, "Measurements of enthalpy in low-density arc- heated flows." **6**, 103–110 (1968).

[12]J. Fay and F. Riddell, "Theory of stagnation point heat transfer in dissociated air," Journal of the Aerospace Sciences **25**, 73–85 (1958).

[13]R. Goulard, "On catalytic recombination rates in hypersonic stagnation heat transfer," **28**, 737–745 (1958).

[14]A. Fagnani, D. Le Quang Huy, B. Helber, S. Demange, A. Turchi, O. Chazot, and A. Hubin, "Investigation of a free-stream air plasma flow by optical emission spectroscopy and comparison to magnetohydrodynamics simulations," in *AIAA Scitech 2020 Forum* (American Institute of Aeronautics and Astronautics, 2020).

[15]D. LeQuang, *Spectroscopic Measurements of Sub- and Supersonic Plasma Flows for the Investigation of Atmospheric Re-Entry Shock Layer Radiation*, Ph.D. thesis, Université Blaise Pascal (2014).

[16]D. Prabhu, D. Saunders, T. Oishi, K. Skokova, J. Santos, J. Fu, I. Terrazas-Salinas, J. Carballo, and D. Driver, "CFD analysis framework for arc-heated flowfields i: Stagnation testing in arc-jets at NASA ARC," in *41st AIAA Thermophysics Conference* (American Institute of Aeronautics and Astronautics, 2009).

[17]O. Chazot, "Experimental Studies on Hypersonic Stagnation Point Chemical Environment," Tech. Rep. (von Karman Institute for Fluid Dynamics, 2006).

[18]T. Gökçen, G. Raiche, D. Driver, J. Balboni, and R. McDaniel, "Applications of CFD analysis

in arc-jet testing of RCC plug repairs," in *25th AIAA Aerodynamic Measurement Technology and Ground Testing Conference* (American Institute of Aeronautics and Astronautics, 2006-06-05).

[19]A. Nawaz, D. Driver, I. Terrazas-Salinas, and S. Sepka, "Surface catalysis and oxidation on stagnation point heat flux measurements in high enthalpy arc jets," in *44th AIAA Thermophysics Conference* (American Institute of Aeronautics and Astronautics, 2013).

[20]A. Viladegut and O. Chazot, "Empirical Modeling of Copper Catalysis for Enthalpy Determination in Plasma Facilities," Journal of Thermophysics and Heat Transfer **34**, 26–36 (2020).

[21]A. Turchi, P. Congedo, and T. Magin, "Thermochemical ablation modeling forward uncertainty analysis—part i: Numerical methods and effect of model parameters," International Journal of Thermal Sciences **118**, 497–509 (2017).

[22]A. Turchi, P. Congedo, B. Helber, and T. Magin, "Thermochemical ablation modeling forward uncertainty analysis—part ii: application to plasma wind-tunnel testing," International Journal of Thermal Sciences **118**, 510–517 (2017).

[23]F. Sanson, F. Panerai, T. Magin, and P. Congedo, "Robust reconstruction of the catalytic properties of thermal protection materials from sparse high-enthalpy facility experimental data," Experimental Thermal and Fluid Science **96** (2018), 10.1016/j.expthermflusci.2018.03.028.

[24]A. del Val, O. Le Maître, P. Congedo, and T. Magin, "Stochastic calibration of a carbon nitridation model from plasma wind tunnel experiments using a bayesian formulation," Carbon **200**, 199–214 (2022).

[25]A. del Val, T. Magin, and P. Congedo, "Quantification of model-form uncertainties affecting the calibration of a carbon nitridation model by means of bayesian model averaging," International Journal of Heat and Mass Transfer **213**, 124271 (2023).

[26]A. del Val, O. Le Maître, T. Magin, O. Chazot, and P. Congedo, "A surrogate-based optimal likelihood function for the Bayesian calibration of catalytic recombination in atmospheric entry protection materials," Applied Mathematical Modelling **101**, 791–810 (2022).

[27]P. Ventura Diaz, A. Parente, J. Meurisse, S. Yoon, and N. Mansour, "High-Fidelity Numerical Analysis of Arc-Jet Aerothermal Environments," in *AIAA Scitech 2020 Forum* (American Institute of Aeronautics and Astronautics, 2020).

[28]A. Brune, T. West, and L. White, "Calibration Probe Uncertainty and Validation for the Hypersonic Material Environmental Test System," Journal of Thermophysics and Heat Transfer **34**, 404–420 (2020).

[29]D. Xiu and G. Karniadakis, ""the wiener–askey polynomial chaos for stochastic differential

equations"," SIAM Journal on Scientific Computing **24**, 619–644 (2002).

[30]J. Sacks, W. Welch, T. Mitchell, and H. Wynn, "Design and analysis of computer experiments," Statistical Science **4**, 409–423 (1989).

[31]A. Forrester, A. Sobester, and A. Keane, *Engineering Design via Surrogate Modelling: A Practical Guide* (Wiley, 2008).

[32]B. Peherstorfer, K. Willcox, and M. Gunzburger, "Survey of Multifidelity Methods in Uncertainty Propagation, Inference, and Optimization," SIAM Review **60**, 550–591 (2018).

[33]M. Giselle Fernández-Godino, C. Park, N. Kim, and R. Haftka, "Issues in deciding whether to use multifidelity surrogates," **57**, 2039–2054 (2019).

[34]Z. Han, C. Xu, L. Zhang, Y. Zhang, K. Zhang, and W. Song, "Efficient aerodynamic shape optimization using variable-fidelity surrogate models and multilevel computational grids," Chinese Journal of Aeronautics **33**, 31–47 (2020).

[35]I. Abdallah, C. Lataniotis, and B. Sudret, "Parametric hierarchical kriging for multi-fidelity aero-servo-elastic simulators — Application to extreme loads on wind turbines," Probabilistic Engineering Mechanics **55**, 67–77 (2019).

[36]H. Babaee, P. Perdikaris, C. Chryssostomidis, and G. E. Karniadakis, "Multi-fidelity modelling of mixed convection based on experimental correlations and numerical simulations," Journal of Fluid Mechanics **809**, 895–917 (2016).

[37]L. Zheng, T. Hedrick, and R. Mittal, "A multi-fidelity modeling approach for evaluation and optimization of wing stroke aerodynamics in flapping flight," Journal of Fluid Mechanics **721**, 118–154 (2013).

[38]A. Sadagopan, D. Huang, U. Duzel, L. Martin, and K. Hanquist, ""assessment of high-temperature effects on hypersonic aerothermoelastic analysis using multi-fidelity multi-variate surrogates"," in *AIAA Scitech 2021 Forum* (American Institute of Aeronautics and Astronautics, 2021).

[39]M. Santos, S. Hosder, and T. West, ""multifidelity turbulent heating prediction of hypersonic inflatable aerodynamic decelerators with surface scalloping"," Journal of Spacecraft and Rockets **58**, 1325–1338 (2021).

[40]K. Quinlan, J. Movva, E. Stein, and A. Kupresanin, "Leveraging multi-fidelity aerodynamic databasing to efficiently represent a hypersonic design space," in *ASCEND 2021* (American Institute of Aeronautics and Astronautics, 2021).

[41]M. Kennedy and A. O'Hagan, "Predicting the Output from a Complex Computer Code When

Fast Approximations Are Available," Biometrika **87**, 1–13 (2000).

[42]A. Forrester, A. Sobester, and A. Keane, "Multi-fidelity optimization via surrogate modelling," Proc. R. Soc. A **463**, 3251–3269 (2007).

[43]Z. Han and S. Görtz, "Hierarchical kriging model for variable-fidelity surrogate modeling," AIAA Journal **50**, 1885–1896 (2012).

[44]V. Picheny, T. Wagner, and D. Ginsbourger, "A benchmark of kriging-based infill criteria for noisy optimization," Structural and Multidisciplinary Optimization **48** (2013), 10.1007/s00158-013-0919-4.

[45]B. Bottin, O. Chazot, M. Carbonaro, V. Haegen, and S. Paris, "The VKI Plasmatron Characteristics and Performance," , 26 (2000).

[46]A. Fagnani, B. Helber, A. Hubin, and O. Chazot, "Line-of-sight gas radiation effects on near-infrared two-color ratio pyrometry measurements during plasma wind tunnel experiments," Measurement **227**, 114175 (2024).

[47]B. Helber, *Material Response Characterization of Low-density Ablators in Atmospheric Entry Plasmas*, Ph.D. thesis, Vrije Universiteit Brussel (2016).

[48]F. Panerai, *Aerothermochemistry Characterization of Thermal Protection Systems*, Ph.D. thesis, Università Degli Studi Di Perugia (2012).

[49]A. Viladegut and O. Chazot, "Catalytic characterization in plasma wind tunnels under the influence of gaseous recombination," Physics of Fluids **34**, 027108 (2022).

[50]A. Fagnani, B. Dias, P. Schrooyen, B. Helber, T. Magin, and O. Chazot, "Investigation of Quartz Ablation in the VKI Plasmatron Facility: Comparison Between Experimental and Numerical Results," in *AIAA AVIATION 2021 FORUM* (American Institute of Aeronautics and Astronautics, 2021).

[51]B. Helber, A. Turchi, and T. Magin, "Determination of active nitridation reaction efficiency of graphite in inductively coupled plasma flows," Carbon **125**, 582–594 (2017).

[52]B. Helber, O. Chazot, A. Hubin, and T. Magin, "Microstructure and gas-surface interaction studies of a low-density carbon-bonded carbon fiber composite in atmospheric entry plasmas," Composites Part A: Applied Science and Manufacturing **72**, 96–107 (2015).

[53]A. Cipullo, B. Helber, F. Panerai, L. Zeni, and O. Chazot, "Investigation of freestream plasma flow produced by inductively coupled plasma wind tunnel," Journal of Thermophysics and Heat Transfer **28**, 381–393 (2014).

[54]F. Panerai and O. Chazot, "Characterization of gas/surface interactions for ceramic matrix com-

posites in high enthalpy, low pressure air flow," Materials Chemistry and Physics **134**, 597–607 (2012).

[55]D. Guariglia, B. Helber, and O. Chazot, "Very high heat-flux measurements in plasmatron with subsonic and supersonic plasma flow," in *8th European Symposium on Aerothermodynamics for Space Vehicles* (European Space Agency, 2015).

[56]B. Helber, A. Turchi, O. Chazot, T. Magin, and A. Hubin, "Gas/Surface Interaction Study of Low-Density Ablators in Sub- and Supersonic Plasmas," in *11th AIAA/ASME Joint Thermophysics and Heat Transfer Conference* (American Institute of Aeronautics and Astronautics, 2014).

[57]N. Metropolis, A. Rosenbluth, M. Rosenbluth, A. Teller, and E. Teller, ""equation of state calculations by fast computing machines"," The Journal of Chemical Physics **21**, 1087–1092 (1953).

[58]W. Hastings, ""monte carlo sampling methods using markov chains and their applications"," Biometrika **57**, 97–109 (1970).

[59]A. Padron, J. Alonso, F. Palacios, M. Barone, and M. Eldred, "Multi-fidelity uncertainty quantification: Application to a vertical axis wind turbine under an extreme gust," in *15th AIAA/ISSMO Multidisciplinary Analysis and Optimization Conference* (American Institute of Aeronautics and Astronautics, 2014).

[60]L. Ng and M. Eldred, "Multifidelity uncertainty quantification using non-intrusive polynomial chaos and stochastic collocation," in *53rd AIAA/ASME/ASCE/AHS/ASC Structures, Structural Dynamics and Materials Conference
20th AIAA/ASME/AHS Adaptive Structures Conference
14th AIAA* (American Institute of Aeronautics and Astronautics, 2012).

[61]M. Eldred, "Recent advances in non-intrusive polynomial chaos and stochastic collocation methods for uncertainty analysis and design," in *50th AIAA/ASME/ASCE/AHS/ASC Structures, Structural Dynamics, and Materials Conference* (American Institute of Aeronautics and Astronautics, 2009).

[62]Y. Zhang, Z. Han, and k. Zhang, "Variable-fidelity expected improvement method for efficient global optimization of expensive functions," Structural and Multidisciplinary Optimization **58** (2018), 10.1007/s00158-018-1971-x.

[63]S. Marelli and B. Sudret, "UQLab: A Framework for Uncertainty Quantification in Matlab," in *Vulnerability, Uncertainty, and Risk* (American Society of Civil Engineers, 2014) pp. 2554–

2563.

[64]C. Lataniotis, S. Marelli, and B. Sudret, "The Gaussian Process Modeling Module in UQLab," (2018).

[65]S. Gordon and J. McBride, "Thermodynamic Data to 20,000 K For Monatomic Gases," Tech. Rep. 1999-208523 (NASA, 1999).

[66]J. Ramshaw, "Self-consistent effective binary interaction approximation for strongly coupled multifluid dynamics," Journal of Non-Equilibrium Thermodynamics **23** (1998), 10.1515/jnet.1998.23.2.135.

[67]R. Gupta, J. Yos, R. Thompson, and K. Lee, "A Review of Reaction Rates and Thermodynamic and Transport Properties for an 11-Species Air Model for Chemical and Thermal Nonequilibrium Calculations to 30000K," Tech. Rep. (NASA, 1990).

[68]C. Park, R. Jaffe, and H. Partridge, "Chemical-Kinetic Parameters of Hyperbolic Earth Entry," Journal of Thermophysics and Heat Transfer **15**, 76–90 (2001).

[69]G. Bellas-Chatzigeorgis, A. Turchi, A. Viladegut, O. Chazot, P. Barbante, and T. Magin, "Development of catalytic and ablative gas-surface interaction models for the simulation of reacting gas mixtures," in *23rd AIAA Computational Fluid Dynamics Conference* (American Institute of Aeronautics and Astronautics, 2017).

[70]J. Scoggins, V. Leroy, G. Bellas-Chatzigeorgis, B. Dias, and T. Magin, "Mutation + + : MUlticomponent Thermodynamic And Transport properties for IONized gases in C++," SoftwareX **12**, 100575 (2020).

[71]G. Candler, H. Johnson, I. Nompelis, V. Gidzak, P. Subbareddy, and M. Barnhardt, "Development of the US3D Code for Advanced Compressible and Reacting Flow Simulations," in *53rd AIAA Aerospace Sciences Meeting* (American Institute of Aeronautics and Astronautics, 2015).

[72]J. Steger and R. Warming, "Flux vector splitting of the inviscid gasdynamic equations with application to finite-difference methods," Journal of Computational Physics **40**, 263–293 (1981).

[73]M. Wright, G. Candler, and M. Prampolini, "Data-parallel lower-upper relaxation method for the navier-stokes equations," AIAA Journal **34**, 1371–1377 (1996).

[74]M. Capriati, K. Prata, T. Schwartzentruber, G. Candler, and T. Magin, "Development of a nitridation gas-surface boundary condition for high-fidelity hypersonic simulations," in *14th WCCM-ECCOMAS Congress* (CIMNE, 2021).

[75]A. Baskaya, M. Capriati, D. Ninni, F. Bonelli, G. Pascazio, A. Turchi, T. Magin, and S. Hickel, "Verification and validation of immersed boundary solvers for hypersonic flows with gas-surface

interactions," in *AIAA AVIATION 2022 Forum* (American Institute of Aeronautics and Astronautics, 2022-06-27).

[76]G. Bellas-Chatzigeorgis, *Development of advanced gas-surface interaction models for chemically reacting flows for re-entry conditions*, Ph.D. thesis, Politecnico di Milano (2018).

[77]L. Eça and M. Hoekstra, "A procedure for the estimation of the numerical uncertainty of CFD calculations based on grid refinement studies," Journal of Computational Physics **262**, 104–130 (2014).

[78]S. Kumar and A. Assam, "Effect of rarefaction on thermal and chemical non-equilibrium for hypersonic flow with different enthalpy and catalytic wall conditions," **15**, 071012 (2023).

[79]Y. Prevereaud, J. Vérant, and J. Annaloro, "Noncatalytic and Finite Catalytic Heating Models for Atmospheric Re-entry Codes," in *First International Orbital Debris Conference (IOC)* (SUGAR LAND, United States, 2019).

[80]K. Sutton and R. Graves, "A general stagnation-point convective heating equation for arbitrary gas mixtures," Tech. Rep. 19720003329 (NASA, 1971).

[81]A. Munafò and T. Magin, "Modeling of stagnation-line nonequilibrium flows by means of quantum based collisional models," Physics of Fluids **26**, 097102 (2014).

[82]A. Gelman and D. Rubin, "Inference from iterative simulation using multiple sequences," Statistical Science **7**, 457–472 (1992).

[83]S. Brooks and A. Gelman, "General methods for monitoring convergence of iterative simulations," Journal of Computational and Graphical Statistics **7**, 434–455 (1998).